One Oxygen Vacancy, Two Charge States: Characterization of Reduced α-MoO_3(010) through Theoretical Methods

Marcos Rellán-Piñeiro and Núria López*

Institute of Chemical Research of Catalonia, ICIQ, and The Barcelona Institute of Science and Technology, BIST, Av. Països Catalans 16, 43007 Tarragona, Spain

Supporting Information

ABSTRACT: Molybdenum oxides are finding increasing applications that rely on their redox character. For the most common polymorph, α-MoO_3, oxygen vacancy formation leaves two electrons on the surface that can be stored as small polarons. Detailed density functional theory calculations that properly account for the self-interaction term, U_{eff} = 3.5 eV, show that the vacancy generates two different configurations: either two Mo^{5+} centers ($Mo^{5+}\square$ and Mo^{5+}=O) or a single double-reduced Mo^{4+}. These states are separated by 0.22 eV with a barrier for interconversion of 0.33 eV, and thus both are populated at catalytic temperatures, as shown by first-principles molecular dynamics. At higher reduction levels, vacancies can only be accumulated along a preferential direction and the energy difference between the 2×Mo^{5+} and Mo^{4+} configurations is reduced. These results point out the need for a revision of the experimental assignments based on our characterization that includes charges, vibrational frequencies, and XPS signatures.

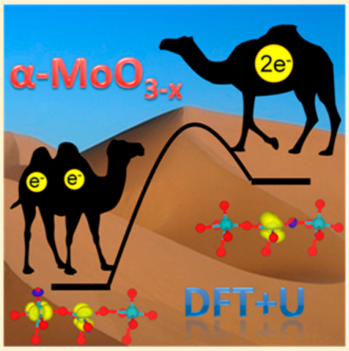

The properties of oxides are dominated by defects, commonly oxygen vacancies.[1,2] Vacancies affect the electronic structure of materials, as the two electrons left upon O removal can be (i) a localized pair at the position of the anion (like for MgO);[3] (ii) separated and localized at the surrounding cations like for TiO_2 and CeO_2 effectively leaving two $M^{(n-1)+}$;[4,5] (iii) partially delocalized between a group of metals, like for In_2O_3.[6,7] Recently, molybdenum oxides have attracted a lot of attention due to their large number of new physical and chemical applications as electro- and chromic devices, in photo-, electro-, and thermal catalysis, in solar cells, and as light-emitting diodes, photodetectors/sensors, batteries, pseudocapacitors, thermoelectric, and ferroelectric materials.[8] All of these applications are based on the versatile geometric (with several structure forms)[9,10] and electronic structure linked to the redox character that can be fine-tuned by the addition of cations[11,12] or hydrogen[13−15] or by oxygen removal,[16] which leads to the formation of Magnéli phases.

In the most common polymorph, α-MoO_3, Mo centers are in the oxidation state Mo^{6+}, and surrounded by oxygen atoms in octahedral environments with a band gap between 3.0 and 3.2 eV.[17−19] α-MoO_3 has an orthorhombic unit cell with *Pbnm* symmetry, where distorted MoO_6 octahedra are ordered in bilayers along the *xz* plane; see Figure 1. van der Waals interactions hold the layered structure packed. There are three nonequivalent oxygen atoms: (i) three coordinated oxygens, O_{3c}, that form a symmetrical bridge along the *x* axis between two Mo centers of the same layer and interact with a sublayer Mo; (ii) asymmetric oxygens, O_b, that bridge two Mo centers along the *z* axis; and (iii) terminal oxygens, O_t, double bonded to only one Mo center present in the interlayer region. Oxygen depletion severely affects the electronic structure of the material, changing its very large work function (~6.9 eV) to lower values ~6.5 eV for a 10% oxygen-deficient material, introducing donor gap states.[20] Upon reduction, the photoemission spectra present additional features: At low vacancy concentrations, these features are assigned to the formation of Mo^{5+} centers, and after a certain concentration, Mo^{4+} features also appear.[20−22] Electron paramagnetic resonance (EPR) studies also indicate the formation of structural point defects of Mo^{5+} close to oxygen vacancies, which at higher concentrations lead to the formation of other centers associated with extended shear structures.[23] Raman vibrational[24] spectroscopy points out the fingerprints for 996, 823 (M=O

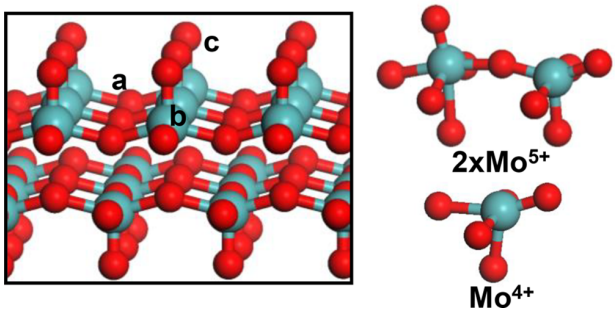

Figure 1. Structures of α-MoO_3(010) pristine surface, left, and local structure of the two possible O_t vacancies, right. (a) O_{3c}, (b) O_b, and (c) O_t. Mo: green and O: red.

asymmetric and symmetric stretchings), and 667 cm^{-1} (asymmetric O−Mo−O). Additional Raman features at 1004 and 1008 cm^{-1} appear at low reduction levels,[25] which disappear at longer reduction times or by hydrogen adsorption and electron beam treatment.[26,27]

Understanding the electronic properties of α-MoO_3 from first-principles[28] has been hampered by the presence of the layered structure, the semiconductor character of the material, and the reducibility of the cation. Hybrid methods have been applied, for instance, to evaluate the vacancy formation energy in the bulk, which is endothermic by 3.68 eV within HSE06.[29] However, the use of these functionals remains unpractical when exploring complex reaction networks on the material. Alternatively, density functional theory (DFT) generalized gradient approximations (GGAs) have been employed. In α-MoO_3 studies with pure GGA functionals,[30−33] electron localization is not found, and thus isolated oxidation states cannot be assigned. The empirical U_{eff} parameter needs to be incorporated to achieve localization.[34] In the literature, scattered U values have been used. Bulk calculations with U_{eff} = 5.0 eV were employed to analyze the preferential oxygen eliminated. O_t was identified as the easiest to remove, but the nature of the charge state was not described.[35] With a value of U_{eff} = 6.3 eV, vacancy formation at O_t position in the bulk leads to a Mo^{4+} center, while the removal of the O_b or O_{3c} lattice oxygen ends up in the formation of two Mo^{5+} centers.[27,36] A recent study with U_{eff} = 6.0 eV suggested the formation of two different states upon reduction, but no characterization was performed, and low vacancy formation energies, ∼1.50 eV, were reported.[37]

In surface models, a value of ∼6 eV was obtained by fitting to hybrids calculations on cluster structure, and it was used by Chen,[38] Asta,[39] and Willock.[40] The latter reported the formation of a Mo^{4+} center. In turn, Metiu[41,42] and Bell[43,44] proposed a U_{eff} value to match the experimental enthalpy of the reaction $MoO_3 + H_2 \rightarrow MoO_2 + H_2O$, but they employed very different values, 2 and 8.6 eV, respectively. Metiu found no localization upon O_t removal and two Mo^{5+} when the vacancy was formed at the O_{3c} position. Therefore, the origin of the different oxidation states observed in experiments cannot be assigned from the previous computational studies.

In this work, we reoptimized the U_{eff} value to describe the reactivity on α-MoO_3(010) accurately following a set of benchmarks that include the comparison to hybrid functionals and CCSD(T) references; see Section S1. Then, we employed PBE+U-D2 to identify the true nature of vacancies in terms of oxidation state of the cations and the corresponding spectroscopic fingerprints.

The bulk PBE-D2 calculated lattice parameters are a = 3.921, b = 14.480, and c = 3.708 Å, in agreement with the experimental values: a = 3.963, b = 13.855, and c = 3.696 Å.[45] Because of the layered packing through dispersion forces along the y axis, the (010) surface is the easiest to cleave. The calculated surface energy was 0.01 eV·$Å^{-2}$ within PBE-D2. The density of states (DOS) of the pristine material shows a small band gap of 1.99 eV with the valence band formed by O(2p) and the conduction band by Mo(4d). The Bader charge analysis of the Mo centers provides a value of 2.63 $|e^-|$, which is well below the formal charge.

Because reduced α-MoO_3 requires the use of PBE+U,[40,44] the U_{eff} value was optimized with two criteria: an electronic term given by electron localization and a thermodynamic one based on reaction energies; see Section S1. Since good thermochemical data are not available, computed values for an acid−base and two redox reactions with the hybrid functional HSE06 were taken as reference. The optimized value for U_{eff} is 3.5 eV (Figure S1). This value also provides the best match in a separate test against the gold standard in molecular chemistry, the CCSD(T) method (Figure S2).

Either the terminal or the two oxygens in the plane surface could be the first ones to be removed. Vacancy (V) formation energies for the reaction $MoO_3 \rightarrow MoO_{3-x} + 1/2\ O_2(g)$ at the O_t position are shown in Figure 2. For the O_t−O_b pair it was

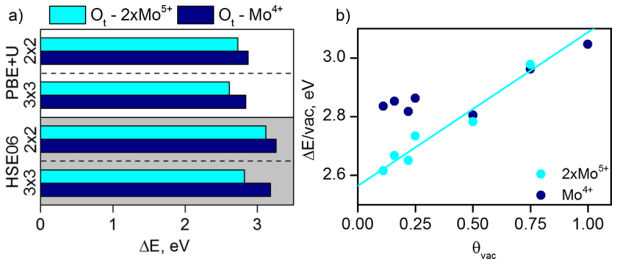

Figure 2. (a) V_{Ot} vacancy formation energy according to the reaction $MoO_3 \rightarrow MoO_{3-x} + 1/2\ O_2(g)$ calculated on the (2 × 2) and (3 × 3) supercells at PBE+U and HSE06 levels. (b) V_{Ot} vacancy formation energy as a function of oxygen depletion for 2×Mo^{5+} and Mo^{4+} states at PBE+U, U_{eff} = 3.5 eV.

found that the calculations within PBE result in similar geometries (the remaining oxygen stays at an intermediate position between that of O_t and O_b) and similar formation energies.[31,32,40] However, in our PBE+U calculations, the converged V_{Ot} geometry keeps the O_b in the surface plane, whereas all of our attempts to converge a V_{Ob} resulted in a displacement of the O_t to the O_b position and the convergence in the same O_t vacancy geometry. Therefore, no vacancies appear at O_b positions on the (010) surface. In turn, the formation of O_t vacancies is endothermic, between 2.61 and 2.87 eV, whereas that of O_{3c} requires an additional 1.80 eV; see Tables S1 and S2. The large difference in energy indicates that vacancies are preferentially formed at O_t positions (V_{Ot}).

V_{Ot} can be present in two different electronic configurations.[37] The ground state has a vacancy formation energy of 2.61 eV (3 × 3 supercell). In the local geometry of this configuration the undercoordinated Mo (Mo_{cus}) cation shortens the long Mo−O_b and the Mo−O_{3c} sublayer bonds by 0.308 and 0.417 Å, whereas its neighboring Mo (still six-fold coordinated) increases Mo−O_b distances by 0.244 and 0.283 Å; see Figure 3. The charge of these two centers differs from that of the pristine surface, 2.48 and 2.49 $|e^-|$ values are retrieved. The DOS in Figure 3 shows how one electron is located in a $d$orbital of each reduced Mo, and the d-orbital of the undercoordinated Mo is lower in energy. The electron magnetization is slightly higher in the undercoordinated center: 0.96 versus 0.83 μ_B. Therefore, this configuration corresponds to Mo^{5+}(□)−O−Mo^{5+}(=O), so both Mo, where the vacancy is created (□), and the neighboring cation, have a 5+ character.

A second configuration with a vacancy formation energy of 2.84 eV has also been obtained. In it, the Mo_{cus}−O bond distances with the oxygens of the surface layer are similar to those of the regular surface, but the Mo atom sinks and reinforces its coordination to O_{3c}, and the distance is shortened by 0.309 Å; see Figure 3. The metal charge is 2.24 $|e^-|$. The DOS clearly shows the localization of the two electrons, with

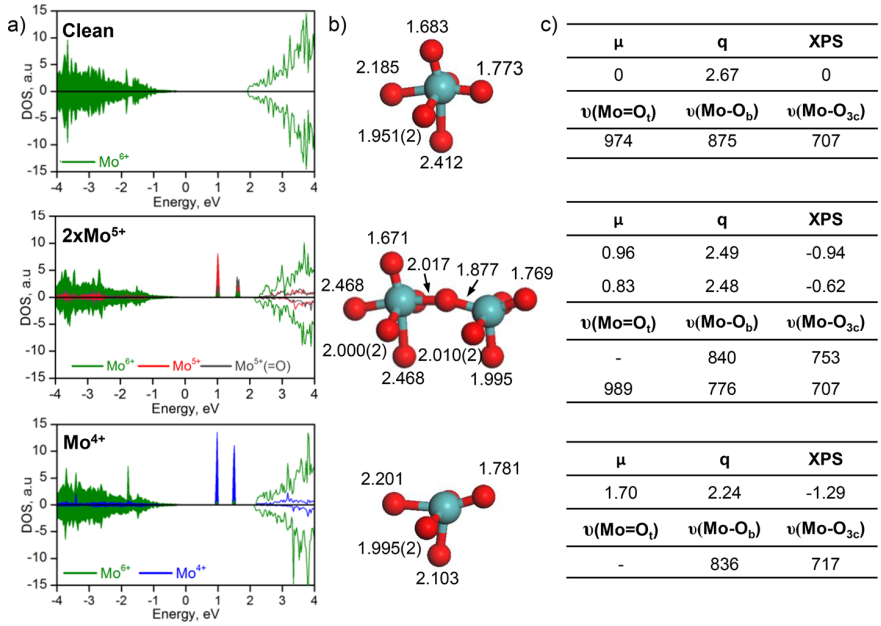

Figure 3. (a) Projected density of states, (b) local geometry with Mo−O bond distances, in angstroms, and (c) fingerprints for the clean surface and the two different states corresponding to the V_{Ot}. Magnetization, μ, in μ_B; Bader charges, q, in $|e^-|$; XPS displacement in eV; and frequencies, υ in cm^{-1}.

the same spin, in two different d orbitals of the Mo^{4+} center, according to the calculated magnetization of 1.70 μ_B. Therefore, this structure is assigned to the formation of a single double-reduced $Mo^{4+}(\square)$ center.

The formation of two different electronic states can be understood as follows. The ground-state $2\times Mo^{5+}$ can disproportionate to Mo^{6+} and Mo^{4+} centers because the relative energies to increase the oxidation state of Mo^{5+} (toward Mo^{6+}) and reduce it (toward Mo^{4+}) cancel each other out. The higher electrostatic interaction between the Mo centers and the surrounding oxygens in the $2\times Mo^{5+}$ is responsible for its larger stability; see Section S3.

Benchmarks performed with the hybrid functional at this concentration (1/9) and the PBE+U geometries lead to a slightly higher vacancy formation energy range: 2.82 and 3.18 eV. The reoptimized PBE+U (U_{eff} = 6.3 eV) energies are much lower, 1.72 and 1.88 eV, but even at these geometries the HSE06 values are 2.93 and 3.30 eV, thus highlighting the critical choice of the U_{eff} when reproducing the formation energies. In summary, the ground state can be identified as a bipolaron, where two electrons are localized on two neighboring Mo centers (Mo^{5+}), whereas the metastable state corresponds to a single dipolaron at the same center (see Figure 4a) and the energy difference is well-represented by PBE+U, U_{eff} = 3.5 eV.

We have inspected how concentration affects the V_{Ot} vacancy formation energies (Figure 2b). $2\times Mo^{5+}$-like defects are increasingly more costly (with a linear dependence on concentration), whereas Mo^{4+} ones are independent of the concentration until coverage reaches 0.5. Moreover, vacancies cannot be accumulated through the [100] direction for both configurations; see Table S1. The origin of this vacancy alignment is at the core of the relaxations observed when the vacancy is formed. When two neighboring vacancies are aligned along [100], the shared O_{3c} sinks toward the subsurface Mo atom (reduces its bond length by 0.1 Å). This ends up

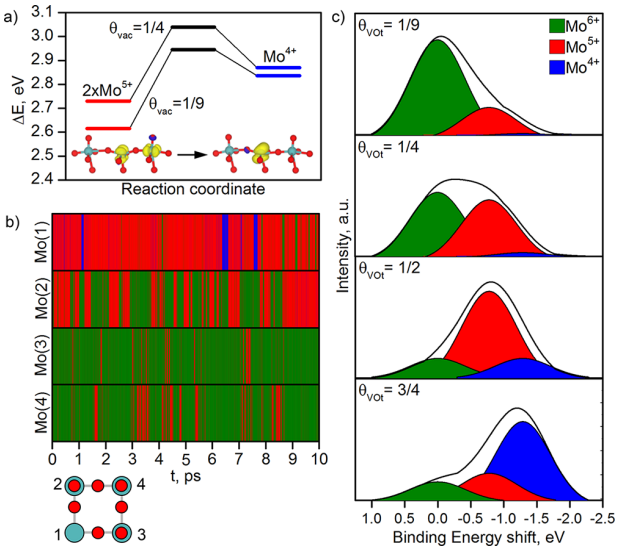

Figure 4. (a) Energy profile for the electron hopping for the conversion $2\times Mo^{5+} \rightarrow Mo^{4+}$ on the (2 × 2) and (3 × 3) supercells and calculated spin density for the two surface states at $0.01e^-Å^{-3}$. (b) Surface Mo local magnetization as a function of time for the molecular dynamics run at 300 °C and θ_{VOt} = 0.25 ML (atom labels shown in the scheme). (c) Calculated XPS at different vacancy coverages, θ_{VOt}, at 350 °C. Green Mo^{6+}, red Mo^{5+}, and blue Mo^{4+}.

increasing the vacancy formation energy. Vacancies would then accumulate on the perpendicular direction, generating crystal shears that induce the formation of Magnéli phases.

Next, we analyzed the interconversion between the two vacancy configurations. α-MoO_3 is known to generate small polarons upon electron addition,[36,39] which are highly mobile, with reported barriers of 0.35 eV in the plane and 0.50 eV between bilayers.[36,39] The CI-NEB results in a barrier for the

conversion between oxidation states $2\times Mo^{5+} \leftrightarrow Mo^{4+}$ of ~0.3 eV, higher within HSE06, 0.40−0.60 eV, but still easy to surmount at reaction temperatures. The barrier is low enough to ensure that the two states are in equilibrium even at room temperature. Therefore, we performed first-principles molecular dynamics (MD) simulations to illustrate the dynamic nature of the electronic states in V_{Ot}. The local magnetization of the surface centers is shown in Figure 4b along the 10 ps trajectory at 300 °C. The main features are that the Mo_{cus} is preferentially Mo^{5+} but also samples Mo^{4+} states and the second polaron is localized either preferentially along the [001] direction or in zigzag but not in the nearest neighbor along the [100] direction. At the temperatures at which α-MoO_3-catalyzed reactions take place (~300 °C), the relative Boltzmann population at low reduction levels (θ_{VOt} = 0.25 ML) is ~93% of Mo^{5+} and ~7% of the Mo^{4+} configuration; from our MD trajectory, these values are 95 and 5%. This is remarkable because experiments have shown that materials reduced at 350 °C and quantified by the XPS fingerprints provide 93:7 Mo^{5+}:Mo^{4+}.[21]

The experimental fingerprints of oxygen-deficient α-MoO_3 can then be reanalyzed considering the dual nature of the vacancies. For instance, the Raman fingerprint of α-MoO_3 has three characteristic bands: Mo═O_t, Mo−O_b and Mo−O_{3c} stretchings at 996, 823, and 667 cm^{-1}, respectively.[46,47] We have calculated the vibrational modes of the different coordination spheres of Mo centers. The reference Mo=O_t is 974 cm^{-1}, which increases by 15 cm^{-1} for the hexacoordinated Mo^{5+} in the $Mo^{5+}(\square)$−O−Mo^{5+}(═O), in agreement with the bands over 1000 cm^{-1} identified in the experiments.[25] In addition, the stretching frequency for Mo−O_b bond is reduced by 35−40 cm^{-1} for undercoordinated cations, and, more importantly, by 100 cm^{-1} for the octahedral Mo^{5+} and therefore could be a fingerprint for this Mo^{5+}(═O) center. The frequency for the Mo−O_{3c} stretching increases for the undercoordinated cations: 10 and 36 cm^{-1} for Mo^{4+} and Mo^{5+}, respectively. Thus this mode can be used to discriminate different states. Complementary, experimental XPS[21,22] on reduced MoO_3 shows the peaks for Mo^{6+}, Mo^{5+}, and Mo^{4+} surface centers. For Mo^{5+} the peaks are displaced around −1.80 eV and for Mo^{4+} −3.00 eV. We calculated the theoretical XPS displacement and obtained values of −0.94 and −1.29 eV for Mo^{5+} and Mo^{4+}, respectively. As shown in Figure 4c, increasing vacancy concentrations would have a dramatic effect on the shape of the XPS spectra.

The ability of the Mo centers to reach different oxidation states can have implications in the chemistry of the oxide. To analyze this we have calculated the adsorption for the two key species in the Formox (methanol to formaldehyde) process.[30] While methanol adsorbs through the hydroxyl to the Mo_{cus} by −1.55 eV in both Mo^{4+} and $2\times Mo^{5+}$; formaldehyde bonds to both Mo_{cus} and an O_b by −1.60 and −1.83 eV for the Mo^{5+} and the Mo^{4+} centers, respectively (see Figure S4). The single-site adsorption by lone-pair donation of methanol is rather independent of the oxidation state of the metal atom. In contrast, the covalent bifunctional coordination of formaldehyde perturbs the structure (for $2\times Mo^{5+}$ the Mo_{cus}−O_b−Mo angle changes from 160 to 155° upon adsorption but does not affect Mo^{4+}), and thus the adsorption energies for the electronic configurations are different.

In summary, a reaction-thermodynamics-adapted PBE+U scheme has been employed to describe the nature of vacancies in α-MoO_3(010). The removal of terminal oxygens generates two different configurations. The ground-state configuration is constituted by two Mo^{5+} polarons that is separated from the metastable configuration with a single Mo^{4+} by 0.2 eV. The interconversion is possible through polaron hopping, and at relevant catalytic temperatures the relative populations are 93:7. Therefore, the complex spectroscopic patterns observed for this material might be due to the different population of ground and metastable states that correspond to a unique type of atom deficiency. This might have implications in the electronic and transport properties, Magnéli phase formation, and chemical properties because the adsorption from the different states can be different. This phenomenon will appear for oxides in which the cations can adopt multiple low oxidation states.

COMPUTATIONAL METHODS

The Vienna Ab Initio Simulation Package (VASP), version 5.3.3, was used to perform the DFT calculations on slabs models.[48,49] PBE[50] with Grimme's semiempiric D2[51] and U approximation[34] (PBE+U-D2) and BEEF-vdW[52] that contains vdW-DF2[53] nonlocal correlation energy were used in the benchmark. In addition, single points with the hybrid HSE06 functional were performed at PBE+U geometries with U_{eff} = 0, 3.5, and 7.0 eV.[54,55] The core electrons were described by the projector-augmented wave (PAW) pseudopotentials[56] (with 14 valence electrons for Mo atoms), and valence ones were expanded in plane waves with a kinetic cutoff energy of 450 eV. Spin polarization was taken into account in all cases.

The bulk was optimized for the PBE functional with a 11 × 3 × 11 k-point mesh and a cutoff energy of 600 eV and employed in all calculations. The (010) surface containing two bilayers was cleaved, and benchmark calculations were performed on a (2 × 2) supercell with a 5 × 5 × 1 k-point sampling. Vacancy formation was studied on a (2 × 2), (3 × 3), (2 × 3), and (3 × 2) supercell with a 3 × 3 × 1, 5 × 5 × 1, 5 × 3 × 1, and 3 × 5 × 1 k-point sampling, respectively. HSE06 single-point calculations were performed with 3 × 3 × 1 k-point mesh for the (2 × 2) supercell and Γ-point sampling for (3 × 3) supercell. During the optimizations, the upper bilayer and adsorbates were relaxed, except where stated otherwise. A vacuum gap of 15 Å was added to prevent the interaction between slabs together with the dipole correction.[57] Complementary, the first-principles MD run was performed in the Born−Oppenheimer approximation on a (2 × 2) supercell with one vacancy defect at 300 °C during 10 ps with 2 ps of equilibration. The most relevant structures have been added to the ioChem-BD database[58] and can be consulted in the following link.[59]

ASSOCIATED CONTENT

Supporting Information

U_{eff} fitting, detailed vacancy formation energies, electrostatic model, adsorption study (PDF)

AUTHOR INFORMATION

Corresponding Author

*E-mail: nlopez@iciq.es.

ORCID

Núria López: 0000-0001-9150-5941

Notes

The authors declare no competing financial interest.

■ ACKNOWLEDGMENTS

We thank the Spanish Ministerio de Economía y Competitividad (MINECO) for financial support (CTQ2015-68770-R, Severo Ochoa Excellence Accreditation 2014−2018 SEV-2013-0319, and Severo Ochoa predoctoral grant SVP-2014-068237). In addition, we thank BSC-RES for providing computational resources. We thank Drs. Marçal Capdevila-Cortada and Hanne Falsig for valuable suggestions.

■ REFERENCES

(1) Pacchioni, G. Oxygen Vacancy: The Invisible Agent on Oxide Surfaces. *ChemPhysChem* **2003**, *4*, 1041−1047.
(2) Henrich, V. E.; Cox, P. A. *The Surface Science of Metal Oxides*; Cambridge University Press: Cambridge, U.K., 1996.
(3) Carrasco, J.; López, N.; Illas, F. First Principles Analysis of the Stability and Diffusion of Oxygen Vacancies in Metal Oxides. *Phys. Rev. Lett.* **2004**, *93*, 225502.
(4) Kowalski, P. M.; Camellone, M. F.; Nair, N. N.; Meyer, B.; Marx, D. Charge Localization Dynamics Induced by Oxygen Vacancies on the TiO_2(110) Surface. *Phys. Rev. Lett.* **2010**, *105*, 146405.
(5) Ganduglia-Pirovano, M. V.; Da Silva, J. L. F.; Sauer, J. Density-Functional Calculations of the Structure of Near-Surface Oxygen Vacancies and Electron Localization on CeO_2(111). *Phys. Rev. Lett.* **2009**, *102*, 026101.
(6) Walsh, A.; Da Silva, J. L. F.; Wei, S.-H.; Körber, C.; Klein, A.; Piper, L. F. J.; DeMasi, A.; Smith, K. E.; Panaccione, G.; Torelli, P.; Payne, D. J.; Bourlange, A.; Egdell, R. G. Nature of the Band Gap In_2O_3 Revealed by First-Principles Calculations and X-Ray Spectroscopy. *Phys. Rev. Lett.* **2008**, *100*, 167402.
(7) Albani, D.; Capdevila-Cortada, M.; Vilé, G.; Mitchell, S.; Martin, O.; López, N.; Pérez-Ramírez, J. Semihydrogenation of Acetylene on Indium Oxide: Proposed Single-Ensemble Catalysis. *Angew. Chem.* **2017**, *129*, 10895−10900.
(8) de Castro, I. A.; Datta, R. S.; Ou, J. Z.; Castellanos-Gomez, A.; Sriram, S.; Daeneke, T.; Kalantar-zadeh, K. Molybdenum Oxides − From Fundamentals to Functionality. *Adv. Mater.* **2017**, *29* (40), 1701619.
(9) Greenwood, N. N.; Earnshaw, A. 23-Chromium, Molybdenum and Tungsten. In *Chemistry of the Elements*, 2nd ed.; Butterworth-Heinemann: Oxford, U.K., 1997; pp 1002−1039.
(10) Goodenough, J. B. *Proc. Climax 4th Intern. Conf. Chemistry and Uses of Molybdenum*; Climax Molybdenum Co.: London, 1982.
(11) Lee, S.-H.; Kim, Y.-H.; Deshpande, R.; Parilla, P. A.; Whitney, E.; Gillaspie, D. T.; Jones, K. M.; Mahan, A. H.; Zhang, S.; Dillon, A. C. Reversible Lithium-Ion Insertion in Molybdenum Oxide Nanoparticles. *Adv. Mater.* **2008**, *20*, 3627−3632.
(12) Hu, X.; Zhang, W.; Liu, X.; Mei, Y.; Huang, Y. Nanostructured Mo-based electrode materials for electrochemical energy storage. *Chem. Soc. Rev.* **2015**, *44*, 2376−2404.
(13) Cheng, H.; Wen, M.; Ma, X.; Kuwahara, Y.; Mori, K.; Dai, Y.; Huang, B.; Yamashita, H. Hydrogen Doped Metal Oxide Semiconductors with Exceptional and Tunable Localized Surface Plasmon Resonances. *J. Am. Chem. Soc.* **2016**, *138*, 9316−9324.
(14) Xie, W.; Su, M.; Zheng, Z.; Wang, Y.; Gong, L.; Xie, F.; Zhang, W.; Luo, Z.; Luo, J.; Liu, P.; Xu, N.; Deng, S.; Chen, H.; Chen, J. Nanoscale Insights into the Hydrogenation Process of Layered α-MoO_3. *ACS Nano* **2016**, *10*, 1662−1670.
(15) Borgschulte, A.; Sambalova, O.; Delmelle, R.; Jenatsch, S.; Hany, R.; Nüesch, F. Hydrogen Reduction of Molybdenum Oxide at Room Temperature. *Sci. Rep.* **2017**, *7*, 40761.
(16) Magneli, A.; Blomberg-Hansson, B.; Kihlborg, L.; Sundkvist, G. Studies on Molybdenum and Molybdenum Wolfram Oxides of the Homologous Series Me_nO_{3n-1}. *Acta Chem. Scand.* **1955**, *9*, 1382−1390.
(17) Bouzidi, A.; Benramdane, N.; Tabet-Derraz, H.; Mathieu, C.; Khelifa, B.; Desfeux, R. Effect of Substrate Temperature on the Structural and Optical Properties of MoO_3 Thin Films Prepared by Spray Pyrolysis Technique. *Mater. Sci. Eng., B* **2003**, *97*, 5−8.
(18) Kröger, M.; Hamwi, S.; Meyer, J.; Riedl, T.; Kowalsky, W.; Kahn, A. P-type Doping of Organic Wide Band Gap Materials by Transition Metal Oxides: A Case-study on Molybdenum Trioxide. Org. *Org. Electron.* **2009**, *10*, 932−938.
(19) Sian, T. S.; Reddy, G. B. Optical, Structural and Photoelectron Spectroscopic Studies on Amorphous and Crystalline Molybdenum Oxide Thin Films. *Sol. Energy Mater. Sol. Cells* **2004**, *82*, 375−386.
(20) Greiner, M. T.; Chai, L.; Helander, M. G.; Tang, W.-M.; Lu, Z.-H. Transition Metal Oxide Work Functions: The Influence of Cation Oxidation State and Oxygen Vacancies. *Adv. Funct. Mater.* **2012**, *22*, 4557−4568.
(21) Zacharopoulou, V.; Vasiliadou, E. S.; Lemonidou, A. A. Exploring the Reaction Pathways of Bioglycerol Hydrodeoxygenation to Propene over Molybdena-based Catalysts. *ChemSusChem* **2018**, *11*, 264−275.
(22) Shetty, M.; Murugappan, K.; Prasomsri, T.; Green, W. H.; Román-Leshkov, Y. Reactivity and Stability Investigation of Supported Molybdenum Oxide Catalysts for The Hydrodeoxygenation (HDO) of m-Cresol. *J. Catal.* **2015**, *331*, 86−97.
(23) Labanowska, M. Paramagnetic Defects in MoO_3−Revisited. *Phys. Chem. Chem. Phys.* **1999**, *1*, 5385−5392.
(24) Py, M. A.; Maschke, K. Intra- and Interlayer Contributions to the Lattice Vibrations in MoO_3. *Physica B+C* **1981**, *105*, 370−374.
(25) Mestl, G.; Verbruggen, N. F. D.; Bosch, E.; Knözinger, H. Mechanically Activated MoO_3. 5. Redox Behavior. *Langmuir* **1996**, *12*, 2961−2968.
(26) Vasilopoulou, M.; Douvas, A. M.; Georgiadou, D. G.; Palilis, L. C.; Kennou, S.; Sygellou, L.; Soultati, A.; Kostis, I.; Papadimitropoulos, G.; Davazoglou, D.; Argitis, P. The Influence of Hydrogenation and Oxygen Vacancies on Molybdenum Oxides Work Function and Gap States for Application in Organic Optoelectronics. *J. Am. Chem. Soc.* **2012**, *134*, 16178−16187.
(27) Hanson, E. D.; Lajaunie, L.; Hao, S.; Myers, B. D.; Shi, F.; Murthy, A. A.; Wolverton, C.; Arenal, R.; Dravid, V. P. Systematic Study of Oxygen Vacancy Tunable Transport Properties of Few-Layer MoO_{3-x} Enabled by Vapor-Based Synthesis. *Adv. Funct. Mater.* **2017**, *27*, 1605380.
(28) Scanlon, D. O.; Watson, G. W.; Payne, D. J.; Atkinson, G. R.; Egdell, R. G.; Law, D. S. L. Theoretical and Experimental Study of the Electronic Structures of MoO_3 and MoO_2. *J. Phys. Chem. C* **2010**, *114*, 4636−4645.
(29) Akande, S. O.; Chroneos, A.; Vasilopoulou, M.; Kennou, S.; Schwingenschlögl, U. Vacancy Formation in MoO_3: Hybrid Density Functional Theory and Photoemission Experiments. *J. Mater. Chem. C* **2016**, *4*, 9526−9531.
(30) Rellán-Piñeiro, M.; López, N. The Active Molybdenum Oxide Phase in the Methanol Oxidation to Formaldehyde (Formox Process): A DFT Study. *ChemSusChem* **2015**, *8*, 2231−2239.
(31) Mei, D.; Karim, A. M.; Wang, Y. Density Functional Theory Study of Acetaldehyde Hydrodeoxygenation on MoO_3. *J. Phys. Chem. C* **2011**, *115*, 8155−8164.
(32) Choksi, T.; Greeley, J. Partial Oxidation of Methanol on MoO_3(010): A DFT and Microkinetic Study. *ACS Catal.* **2016**, *6*, 7260−7277.
(33) Shetty, M.; Buesser, B.; Román-Leshkov, Y.; Green, W. H. Computational Investigation on Hydrodeoxygenation (HDO) of Acetone to Propylene on α-MoO_3(010) Surface. *J. Phys. Chem. C* **2017**, *121*, 17848−17855.
(34) Dudarev, S. L.; Botton, G. A.; Savrasov, S. Y.; Humphreys, C. J.; Sutton, A. P. Electron-energy-loss Spectra and the Structural Stability of Nickel Oxide: An LSDA+U study. *Phys. Rev. B: Condens. Matter Mater. Phys.* **1998**, *57*, 1505−1509.
(35) Inzani, K.; Grande, T.; Vullum-Bruer, F.; Selbach, S. M. A van der Waals Density Functional Study of MoO_3 and Its Oxygen Vacancies. *J. Phys. Chem. C* **2016**, *120*, 8959−8968.
(36) Tahini, H. A.; Tan, X.; Lou, S. N.; Scott, J.; Amal, R.; Ng, Y. H.; Smith, S. C. Mobile Polaronic States in α-MoO_3: An ab Initio Investigation of the Role of Oxygen Vacancies and Alkali Ions. *ACS Appl. Mater. Interfaces* **2016**, *8*, 10911−10917.

(37) Kim, H. S.; Cook, J. B.; Lin, H.; Ko, J. S.; Tolbert, S. H.; Ozolins, V.; Dunn, B. Oxygen Vacancies Enhance Pseudocapacitive Charge Storage Properties of MoO_{3-x}. *Nat. Mater.* **2017**, *16*, 454.
(38) Lei, Y.-H.; Chen, Z.-X. DFT+U Study of Properties of MoO_3 and Hydrogen Adsorption on MoO_3(010). *J. Phys. Chem. C* **2012**, *116*, 25757−25764.
(39) Ding, H.; Lin, H.; Sadigh, B.; Zhou, F.; Ozoliņš, V.; Asta, M. Computational Investigation of Electron Small Polarons in α-MoO_3. *J. Phys. Chem. C* **2014**, *118*, 15565−15572.
(40) Coquet, R.; Willock, D. J. The (010) surface of α-MoO_3, a DFT + U study. *Phys. Chem. Chem. Phys.* **2005**, *7*, 3819−3828.
(41) Agarwal, V.; Metiu, H. Energy of Oxygen-Vacancy Formation on Oxide Surfaces: Role of the Spatial Distribution. *J. Phys. Chem. C* **2016**, *120*, 2320−2323.
(42) Agarwal, V.; Metiu, H. Oxygen Vacancy Formation on α-MoO_3 Slabs and Ribbons. *J. Phys. Chem. C* **2016**, *120*, 19252−19264.
(43) Lutfalla, S.; Shapovalov, V.; Bell, A. T. Calibration of the DFT/GGA+U Method for Determination of Reduction Energies for Transition and Rare Earth Metal Oxides of Ti, V, Mo, and Ce. *J. Chem. Theory Comput.* **2011**, *7*, 2218−2223.
(44) Getsoian, A. B.; Bell, A. T. The Influence of Functionals on Density Functional Theory Calculations of the Properties of Reducible Transition Metal Oxide Catalysts. *J. Phys. Chem. C* **2013**, *117*, 25562−25578.
(45) Kihlborg, L. Least-squares Refinement of the Crystal Structure of Mo Trioxide. *Ark. Kemi* **1963**, *21*, 357−64.
(46) Camacho-López, M. A.; Escobar-Alarcón, L.; Picquart, M.; Arroyo, R.; Córdoba, G.; Haro-Poniatowski, E. Micro-Raman Study of the m-MoO_2 to α-MoO_3 Transformation Induced by cw-laser Irradiation. *Opt. Mater.* **2011**, *33*, 480−484.
(47) Dieterle, M.; Weinberg, G.; Mestl, G. Raman spectroscopy of molybdenum oxides Part I. Structural Characterization of Oxygen Defects in MoO_{3-x} by DR UV/VIS, Raman Spectroscopy and X-ray Diffraction. *Phys. Chem. Chem. Phys.* **2002**, *4*, 812−821.
(48) Kresse, G.; Furthmüller, J. Efficient Iterative Schemes for *ab initio* Total-energy Calculations Using a Plane-wave Basis Set. *Phys. Rev. B: Condens. Matter Mater. Phys.* **1996**, *54*, 11169−11186.
(49) Kresse, G.; Furthmüller, J. Efficiency of *ab-initio* Total Energy Calculations for Metals and Semiconductors Using a Plane-wave Basis Set. *Comput. Mater. Sci.* **1996**, *6*, 15−50.
(50) Perdew, J. P.; Burke, K.; Ernzerhof, M. Generalized Gradient Approximation Made Simple. *Phys. Rev. Lett.* **1996**, *77*, 3865−3868.
(51) Grimme, S. Semiempirical GGA-type Density Functional Constructed with a Long-range Dispersion Correction. *J. Comput. Chem.* **2006**, *27*, 1787−1799.
(52) Wellendorff, J.; Lundgaard, K. T.; Møgelhøj, A.; Petzold, V.; Landis, D. D.; Nørskov, J. K.; Bligaard, T.; Jacobsen, K. W. Density Functionals for Surface Science: Exchange-correlation Model Development with Bayesian Error Estimation. *Phys. Rev. B: Condens. Matter Mater. Phys.* **2012**, *85*, 235149.
(53) Lee, K.; Murray, É. D.; Kong, L.; Lundqvist, B. I.; Langreth, D. C. Higher-accuracy van der Waals Density Functional. *Phys. Rev. B: Condens. Matter Mater. Phys.* **2010**, *82*, 081101.
(54) Heyd, J.; Scuseria, G. E.; Ernzerhof, M. Hybrid Functionals Based on a Screened Coulomb Potential. *J. Chem. Phys.* **2003**, *118*, 8207−8215.
(55) Paier, J.; Marsman, M.; Hummer, K.; Kresse, G.; Gerber, I. C.; Ángyán, J. G. Erratum: "Screened Hybrid Density Functionals Applied to Solids" [J. Chem. Phys. 124, 154709 (2006)]. *J. Chem. Phys.* **2006**, *125*, 249901.
(56) Kresse, G.; Joubert, D. From Ultrasoft Pseudopotentials to the Projector Augmented-wave Method. *Phys. Rev. B: Condens. Matter Mater. Phys.* **1999**, *59*, 1758−1775.
(57) Makov, G.; Payne, M. C. Periodic Boundary Conditions in *ab initio* Calculations. *Phys. Rev. B: Condens. Matter Mater. Phys.* **1995**, *51*, 4014−4022.
(58) Álvarez-Moreno, M.; de Graaf, C.; López, N.; Maseras, F.; Poblet, J. M.; Bo, C. Managing the Computational Chemistry Big Data Problem: The ioChem-BD Platform. *J. Chem. Inf. Model.* **2015**, *55* (1), 95−103.
(59) Rellán-Piñeiro, M.; López, N. *Data Set for One Oxygen Vacancy, Two Charge States: Characterization of Reduced α-MoO_3(010) through Theoretical Methods*. DOI: 10.19061/iochem-bd-1-59.